

The power spectrum of the flux distribution in the Lyman- α forest of a Large sample of UVES QSO Absorption Spectra (LUQAS)^{*}

T.-S. Kim¹, M. Viel¹, M.G. Haehnelt¹, R.F. Carswell¹, S. Cristiani²

¹ *Institute of Astronomy, Madingley Road, Cambridge CB3 0HA*

² *INAF-Osservatorio Astronomico di Trieste, via G.B. Tiepolo 11, I-34131 Trieste, Italy*

submitted 4 April 2003

ABSTRACT

The flux power spectra of the Lyman- α forest from a sample of 27 QSOs taken with the high resolution echelle spectrograph UVES on VLT are presented. We find a similar fluctuation amplitude at the peak of the “3D” flux power spectrum at $k \sim 0.03$ s/km as the study by Croft et al. (2002), in the same redshift range. The amplitude of the flux power spectrum increases with decreasing redshift if corrected for the increase in the mean flux level as expected if the evolution of the flux power spectrum is sensitive to the gravitational growth of matter density fluctuations. This is in agreement with the findings of McDonald et al. (2000) at larger redshift. The logarithmic slope of the “3D” flux power spectrum, $P_F(k)$, at large scales $k < 0.03$ s/km, is 1.4 ± 0.3 *i.e.* 0.3 shallower than that found by Croft et al. 2002 but consistent within the errors.

Key words: Cosmology: intergalactic medium – large-scale structure of universe – quasars: absorption lines

1 INTRODUCTION

The prominent absorption features blueward of the Lyman- α emission in the spectra of high-redshift quasars (QSOs) are now generally believed to arise from smooth density fluctuations of a photoionized warm intergalactic medium. Support for the hypothesis that such a fluctuating Gunn-Peterson effect (Gunn & Peterson 1965) is responsible for the Lyman- α forest comes from a detailed comparison of analytical calculations (e.g. Bi & Davidsen 1997; Viel et al. 2002a; Matarrese & Mohayaee 2002) and numerical simulations (Cen et al. 1994; Zhang, Anninos & Norman 1995; Miralda-Escudé et al. 1996; Hernquist et al. 1996, Theuns et al. 1998, 2002; Meiksin, Bryan & Machacek 2001) with observed absorption spectra (see Rauch 1998 for a review; Kim et al. 2002). The numerical simulations have thereby demonstrated convincingly that the fluctuations in the Lyman- α optical depth should reflect the density of the dark matter (DM) distribution on scales larger than a “filtering” scale related to the Jeans length (Gnedin & Hui 1998; Viel et al. 2002b). This still rather new paradigm for the origin of the Lyman- α forest has led to considerable interest in using QSO absorption spectra to study the dark matter distribution. Of particular interest is thereby the possibility to probe the density fluctuation of matter with the flux power spectrum of QSO absorption lines. The first study of Croft et al. (1998) was followed by further investigations by Croft et al. (1999b, 2002; hereafter C99 and C02) and McDonald et al. (2000; hereafter M00). These studies compared the observed flux power spectrum to that obtained from numerically simulated absorption spectra in order to constrain the slope and amplitude of the linear dark matter power spectrum for wave numbers in the range 0.002 s/km $< k < 0.05$ s/km. This corresponds to wavelength of about $1 h^{-1}$ Mpc to $50 h^{-1}$ Mpc (comoving) at redshift 2–4 and extends to scales considerably smaller than those accessible

^{*} Based on data taken from the ESO archive obtained with UVES at VLT, Paranal, Chile.

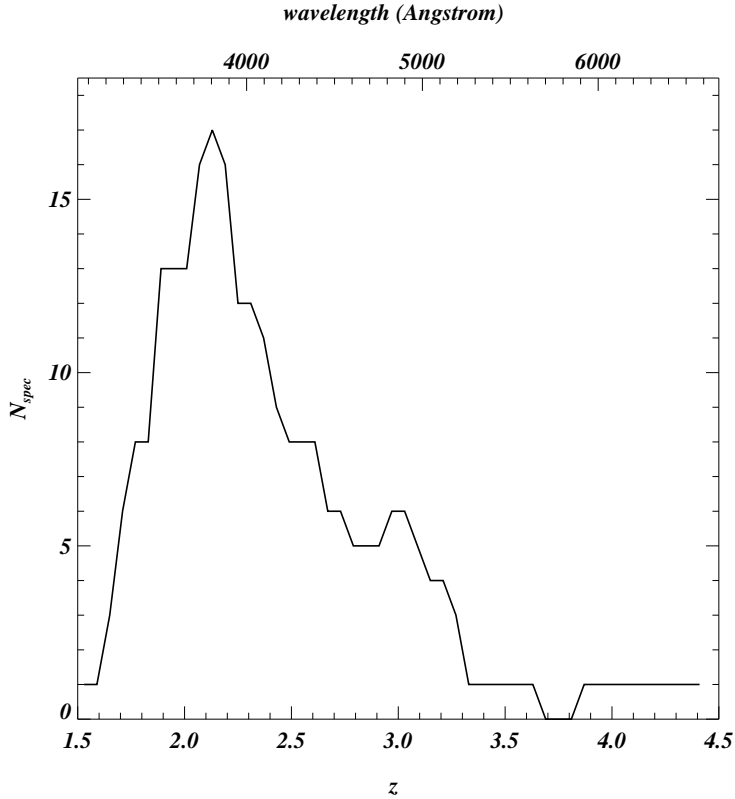


Figure 1. Number of spectra for which the Lyman- α absorption region covers a given redshift (bottom axis) and wavelength (top axis). The median redshift of the whole sample is $z = 2.25$. The total redshift path is $\Delta z = 13.75$.

by galaxy surveys. At these small scales the matter power spectrum is sensitive to a possible cut-off expected if the DM were warm dark matter (Narayanan et al. 2000) and gives constraints on the matter fraction in neutrinos (Croft et al. 1999a; Elgaroy et al. 2002). The redshift range probed is intermediate between that probed by the CMB and galaxy surveys and allows to investigate the gravitational growth of structure and possibly the redshift evolution of dark energy (Seljak et al. 2002; Viel et al. 2003a). C99 inferred an amplitude and slope which was consistent with a COBE normalized Λ CDM model with a primordial scale invariant fluctuation spectrum (Phillips et al. 2001). However, M00 and C02, using a larger sample of better quality data, found a somewhat shallower slope and smaller fluctuation amplitude. The later data have been claimed to be in (mild) conflict with a primordial scale-invariant, CMB-normalized fluctuation spectrum and has been used to argue for a running spectral index (Bennet et al. 2003; Spergel et al. 2003; Verde et al. 2003). However, inferring the matter power spectrum from the flux power spectrum is a non-trivial matter (Zaldarriaga, Hui & Tegmark, 2001; Gnedin & Hamilton 2002). In particular, Zaldarriaga et al. (2003) and Seljak et al. (2003) have argued that C02 underestimated the error in the mean flux decrement and therefore underestimated the errors in the slope and amplitude of the matter power spectrum. There is thus considerable interest in further theoretical study and accurate observational determination of the Lyman- α forest flux power spectrum. We present here the flux power spectra of a new large sample of 27 high-resolution absorption spectra taken with the high-resolution, high S/N spectrograph on VLT (the LUQAS sample). The bispectrum of the flux for the LUQAS sample has been investigated in Viel et al. (2003c).

The sample and the data reduction are presented in Section 2. Section 3 describes how we calculate the flux power spectra. Section 4 contains our results and in section 5 we give a comparison to previous published flux power spectra. In section 6 we briefly discuss implications of our results for the power spectrum of matter density fluctuations and in section 7 we give our conclusions. We will assume $\Omega_m = 0.3$, $\Omega_\Lambda = 0.7$ throughout the paper.

2 THE DATA

2.1 Description of the sample

The sample consists of 27 spectra taken with the Ultra-Violet Echelle Spectrograph (UVES) on VLT, Paranal, Chile, over the period 1999–2002. The 27 spectra were taken from the ESO archive and are publicly available to the ESO community. We have selected the QSO sample based on the following criteria: 1) S/N larger than 25 in the Lyman- α forest region; 2) complete or nearly complete coverage of the Lyman- α forest region; 3) few damped Lyman- α systems and sub-DLAs (column density $10^{(19.5-20.3)} \text{ cm}^{-2}$) in the Lyman- α forest region; 4) no broad absorption line systems; 5) publicly available as of January 1, 2003. Table 1 lists the observation log for the LUQAS sample including the name and redshift of the targets and program ID. Only relevant observations are listed. The total redshift path of the sample is $\Delta z = 13.75$. In Figure 1 we plot the number of spectra covering a given redshift (bottom axis) and wavelength (top axis). The median redshift of the sample is $\langle z \rangle = 2.25$ and the number of spectra covering the median redshift is 17. In Table 2 we list the Lyman- α redshift range, wavelength range, and signal-to-noise ratio for all the spectra of our sample. There is no overlap with published samples for which the flux power spectrum has been calculated.

2.2 Data reduction

The data were reduced with the ECHELLE/UVES environment of the software package MIDAS. Since the release of the first version of UVES/MIDAS in 1999, there have been several upgrades. Version 1.2.0 was released in September 2001 and the most up-to-date version is 1.4.0 which became available with the MIDAS version released in September 2002. The sample presented here was reduced with different versions of UVES/MIDAS as indicated in Table 1. The 8 spectra marked with “K” have been reduced as in Kim et al. (2002) and the reader is referred to this paper for details. The spectra marked with “O” and “N” are reduced with versions, 1.2.0 and 1.4.0, respectively, as described in this section. To ensure that the quality of the reduction is sufficiently homogeneous for our purposes we have compared the results from different versions of the extraction procedure. The newest version (1.4.0) gives a slightly better S/N than the older versions. Overall, however, the differences are negligible.

Cosmic rays were flagged using a median filter and the wavelength calibration was done using the ThAr lamp. After the bias and inter-order background are subtracted, the optimal extraction procedure of REDUCE/UVES fits the individual orders of the echelle spectrum with a Gaussian distribution along the spatial direction. The sky background is thereby treated as the base of the Gaussian fit. In this way the sky background is subtracted and an optimal extraction of the QSO spectrum is achieved (Kim et al. 2001). This usually works except in regions with saturated absorption. Saturated absorption lines are not distinguishable from the sky background in the 2-dimensional pre-extracted CCD frames. This causes badly fitted Gaussian profiles for CCD columns containing regions of saturated absorption. This leads to an underestimate of the sky background and results in flux levels larger than zero for saturated lines. The level of the underestimated sky subtraction varies from frame to frame and from wavelength to wavelength. It occasionally reaches up to 5%. There is no systematic way to quantify this effect, except that the sky background subtraction is worse at short wavelengths, in particular at wavelengths shorter than 3400 Å. We did not try to correct the zero-level with a fixed offset.

Standard stars, observed during the same nights, were mainly selected from the Kitt Peak IIDS Standard Star Manual and their spectra were reduced in the same way as the QSO spectra. This was done for each night separately to correct for the blaze function due to the instrument sensitivity. Unfortunately, most of the standard stars (as the QSOs) do not have flux calibrated points below 3300 Å. Consequently we had to extrapolate the flux calibration below 3300 Å. We also found many standard stars to have many absorption lines at this very high resolution. With calibrated data points sampled at every 50 Å to 100 Å (larger than a typical one echelle order ~ 40 Å), it is not always possible to correct for the blaze function. For the QSOs for which observations were spread over a period of one year problems occurred with the correction for the shape of the blaze function below 3300 Å. Here the flat-field lamp starts to show a non-flat feature and the detector sensitivity decreases very rapidly. The flux distributions of the standard stars and the QSOs are also quite different. These problems result in a smoothly varying feature in the continuum of the merged spectrum. This varying “continuum feature” can, however, be removed by careful continuum fitting.

Where possible, each order of the extracted spectrum was corrected for the blaze function. The corrected order was then cut at both ends where the flat field errors are rapidly increasing. Finally the orders were merged with weights chosen to maximize the resultant signal-to-noise ratio. QSOs for which the blaze function correction was not possible suffer from larger continuum fitting errors below ~ 3400 Å (corresponding to $z_{Ly\alpha} \leq 1.8$). The LUQAS sample, however, covers mainly redshifts larger than 1.8.

In the final merged spectrum the individual extractions are weighted corresponding to their S/N and resampled with 0.05 Å binning. The resolving power is ~ 45000 in the regions of interest. The wavelengths in the final spectra

Table 1. Observation Log

QSO	V^a	z_{em}^b	Setting	Exptime (secs)	Program ID ^c	UVES/MIDAS ^d
HE0001–2340	16.7	2.259	dic1 346X580	21600	160.A-0106	N
			dic2 437X860	21600		
Q0002–422	17.5	2.659	dic1 346X580	28800	160.A-0106	N
			dic2 437X860	39600		
Q0055–269	17.9	3.656	dic1 346X580	25200	65.O-0296	K2
			dic2 437X860	21600		
Q0103–260	18.3	3.371	Red 520	24800	66.A-0133	O
Q0109–3518	16.6	2.405	dic1 346X580	25200	160.A-0106	O
			dic2 437X860	21600		
Q0122–380	17.1	2.192	dic1 346X580	21600	160.A-0106	O
HE0151–4326		2.784	dic1 346X580	28800	160.A-0106	N
			dic2 437X860	32400		
PKS0237–23	16.8	2.223	dic1 346X580	21600	160.A-0106	N
			dic2 437X860	21600		
Q0302–003	18.4	3.284	dic1 346X580	20000	Comm.	K2
PKS0329–255	17.1	2.707	dic1 346X580	46800	160.A-0106	N
			dic2 437X860	39600		
Q0329–385	17.2	2.435	dic1 346X580	21600	160.A-0106	O
			dic2 437X860	21600		
Q0420–388	16.9	3.117	dic1 390X564	28800	160.A-0106	N
			dic2 437X860	28800		
Q0453–423	17.3	2.657	dic1 346X580	28800	160.A-0106	N
			dic2 437X860	28800		
HE0515–4414	14.9	1.718	dic1 346X580	19000	Comm.	K1
HE0940–1050	16.6	3.083	dic1 346X580	18000	160.A-0106 &	N
			dic2 437X860	14400	65.O-0474	
Q1101–264	16.0	2.141	dic1 346X580	23400	SV	K2
HE1104-1805A	17.9	2.315	Blue 360	6578	Comm.	O
			dic1 346X564	11400	67.A-0278	
			dic1 390X580	7600		
			dic2 437X860	26100		
HE1122–1648	17.7	2.405	dic1 346X580	26400	SV	K2
			dic2 437X860	27000		
HE1158–1843	16.9	2.448	dic1 346X580	21600	160.A-0106	N
			dic2 437X860	21600		
HE1341–1020	17.1	2.135	dic1 346X580	32400	160.A-0106	O
HE1347–2457		2.616	dic1 346X580	21044	SV, 160.A-0106	K2, N
			dic2 437X860	32400		
PKS1448–232	17.0	2.218	dic1 346X580	28800	160.A-0106	N
			dic2 437X860	21600		
Q1451–15		4.762	Red 580	36000	160.A-0106	N
			dic2 437X860	28800		N
PKS2126–158	17.3	3.280	dic1 390X564	32400	160.A-0106	O
			dic2 437X860	28800		
HE2217–2818	16.0	2.413	dic1 346X580	16200	Comm.	K1
			dic1 390X564	10800		
J2233–606	17.5	2.251	dic1 346X580	28800	Comm.	K1
			dic2 437X860	21600		
HE2347–4342	16.3	2.880	dic1 346X580	21600	160.A-0106	O
			dic2 437X860	28800		

^a Taken from the Simbad Database. The blank fields indicate that there is no information of such fields in the Simbad Database.^b Estimated from the spectrum.^c SV: Science Verification in Feb., 2000. Comm: UVES Commissioning in Sep.-Oct., 1999. Prog ID: 160.A-0106: The QSO public survey: The cosmic evolution of the intergalactic medium (PI: J. Bergeron). Prog ID: 65.O-0296: A study of the IGM-galaxy connection at $z \sim 3$ (PI: S. D’Odorico). Prog ID: 65.O-0474: Deuterium abundance in the high redshift QSO system towards HE0940–1050 (PI: P. Molaro). Prog ID: 66.A-0133: The nature of the Lyman- α forest of Q0103–260 (PI: D. Appenzeller). Prog ID: 67.A-0278: Testing the enrichment mechanism of the IGM through the study of small scale variations in the metal content of the $z \sim 2$ Ly α forest.^d K1: Kim et al. (2001), K2: Kim et al. (2002), O: the 1.2.0 UVES/MIDAS version, N: the 1.4.0 UVES/MIDAS version

Table 2. Analyzed QSOs

QSO	$z_{\text{Ly}\alpha}$	$\lambda_{\text{Ly}\alpha}(\text{\AA})$	S/N per pixel ^a	metals ^b	notes ^c
HE0001–2340	1.75–2.23	3345–3922	50–70		DLA at 3873.1 \AA
Q0002–422	2.09–2.62	3755–4404	35–65		
Q0055–269	2.93–3.61	4778–5603	30–75	fitted	
Q0103–260	2.72–3.24	4522–5156	~ 25		gap: 5156–5239 \AA
Q0109–3518	1.87–2.37	3495–4098	50–70		
Q0122–380	1.69–2.16	3276–3841	40–70	fitted	
HE0151–4326	2.19–2.75	3883–4554	50–80		
PKS0237–23	1.73–2.19	3319–3879	55–75		AS at 3934.5 \AA
Q0302–003	2.95–3.24	4807–5156	30–60	fitted	
PKS0329–255	2.13–2.67	3808–4461	25–30		AS at 4513.7 \AA
Q0329–385	1.90–2.40	3525–4131	30–55	fitted	
Q0420–388	2.48–3.08	4230–4955	60–100		DLA at 4968.5 \AA , AS at 5013.6 \AA
Q0453–423	2.09–2.62	3753–4401	50–70		DLA at 4016 \AA
HE0515–4414	1.53–1.69	3080–3271	30–90	fitted	
HE0940–1050	2.45–3.04	4190–4914	60–90		
Q1101–264	1.65–2.11	3224–3780	30–70	fitted	sub-DLA at 3450 \AA
HE1104–185	1.80–2.23	3402–3989	30–60	fitted	
HE1122–1648	1.88–2.37	3507–4098	35–65	fitted	AS at 4156.7 \AA
HE1158–1843	1.91–2.41	3544–4150	30–50		AS at 4200 \AA
HE1341–1020	1.66–2.10	3227–3773	30–55		AS at 3826 \AA
HE1347–2457	2.05–2.57	3711–4352	50–70	fitted	
PKS1448–232	1.72–2.18	3303–3873	30–60		
Q1451–15	3.86–4.70	5912–6934	35–60		
PKS2126–158	2.61–3.23	4392–5151	50–100	fitted	
HE2217–2818	1.88–2.38	3503–4107	35–60	fitted	
J2233–606	1.74–2.22	3337–3912	30–50	fitted	
HE2347–4342	2.29–2.84	4002–4669	40–60	fitted	AS at 4744.3 \AA

^a The signal-to-noise ratio varies across the spectrum. The listed S/N is estimated in regions without strong absorption. The S/N usually increases towards longer wavelengths. In the case of very high S/N the QSOs usually have a prominent Ly α emission line. These values are meant as a rough indication of the quality of the spectrum.

^b We specify for which QSO metals lines have been fitted (see text for the details).

^c We identify DLAs (damped Lyman- α systems), AS (associated systems) and gaps in the spectra only when these systems affect the Ly α forest regions considered in the study.

are vacuum heliocentric. The S/N generally increases towards longer wavelengths. Table 2 lists the typical S/N of each QSO spectrum and the Lyman- α wavelength and redshift ranges.

2.3 Continuum fitting

Unfortunately, there is no objective way to fit the continuum. The spectra were broken into parts. For these a continuum was fitted with 5th and 7th order polynomials by choosing regions devoid of absorptions (for more details, see Kim et al. (2001, 2002)). When we split the spectrum into sections for the continuum fitting occasionally there is a mismatch in the overlap regions of the continuum fit. The overlap regions of echelle orders can also be problematic. In these cases we adjust the continuum manually to achieve a smooth continuum which is still an acceptable fit to the data. At $z \sim 2.5$ there are about 3-5 such problematic regions in the Lyman- α forest in each object.

As we will discuss in more detail in Section 3.4. continuum fitting is the limiting factor in using flux power spectra to constrain fluctuations of the matter density on large scales. Note also that due to the imperfect blaze function correction of the data for echelle spectra the quality of the continuum fit will never be very good over scales larger than one echelle order, typically 30–40 \AA for UVES spectra. Continuum fitting is no doubt somewhat arbitrary. We have therefore also employed a simple averaging method originally suggested by C02. This method is a modification of the trend removal technique proposed by Hui et al. (2001). In section 3 we will use spectra processed in this way to demonstrate some effects of the continuum fitting on the flux power spectrum.

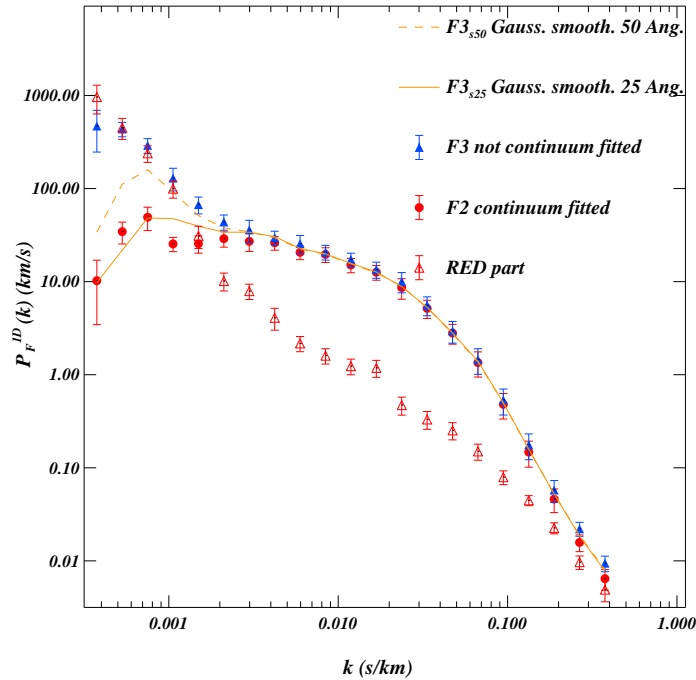


Figure 2. Effect of continuum fitting on the 1D flux power spectrum. Circles are for the continuum fitted spectrum $F2 = e^{-\tau} / \langle e^{-\tau} \rangle - 1$, solid triangles are for the not continuum fitted spectrum $F3 = I_{\text{obs}} / \langle I_{\text{obs}} \rangle - 1$. Dashed and solid line are for spectra smoothed with a Gaussian window of 25 and 50 Å width, respectively, as described in the text. Error bars denote the 1σ errors of the mean values. Open triangles show the flux power spectrum of $F3$ for the region redwards of the Lyman- α emission line (1265.67 - 1393.67 Å).

2.4 Damped Lyman- α systems, associated systems and metal lines

Here we are interested only in the Lyman- α forest and only consider the wavelength range between the Ly α and Ly β emission lines of the QSO. To avoid effects due to the enhanced ionizing flux close to the QSO (proximity effect), we consider only the Ly α forest region more than 3000 km s $^{-1}$ shortward of the Ly α emission.

There are a number of “contaminants” which may contribute to the flux power spectrum on the scales investigated here, most notably DLAs, associated systems (AS) and metal line systems. DLAs and sub-DLAs are easily identified in the spectra. We report in Table 2 the central wavelength of the DLAs found in the Lyman- α regions out of the 27 spectra. We remove a region of 100 Å centered on each damped Lyman- α system when we calculate the flux power spectrum.

Most QSOs in Table 1 show associated systems, *i.e.* absorption systems at redshifts very close or higher than the QSO emission redshift. Very strong ASs have been found in 6 spectra, which show non-negligible Ly β absorption lines at wavelength shorter than the QSO Lyman- β emission line. For these QSOs we increase the minimum wavelength of the Lyman- α range used to exclude the Ly β absorption due to ASs.

Full absorption line lists were available for 8 QSOs of the sample (marked as “K” in Table 1; Kim et al. 2001, 2002) and we have fitted the metal lines of five more QSOs using VPFIT (Carswell et al.: <http://www.ast.cam.ac.uk/~rfc/vpfit.html>). We expect that less than 5% of all metal lines (usually very narrow lines) remained unidentified, and that the residual contamination of the pixel sample by unidentified metal lines is smaller than 0.3%. In section 3.4 we will use the 13 QSOs for which the metal lines were fitted to estimate the metal line contribution to the flux power spectrum.

3 CALCULATING THE FLUX POWER SPECTRA

3.1 Basic formulae

The observed intensity is related to the emitted intensity through the optical depth, τ , as follows

$$I_{\text{obs}} = I_{\text{em}} e^{-\tau}. \quad (1)$$

The fluctuations in the observed intensity are thus a superposition of the fluctuations of the emitted intensity and those of the absorption optical depth which reflects the density fluctuations of the underlying matter distribution. As we will discuss in more detail below continuum fluctuations start to contribute significantly on scales $k < k_{\text{cont}} \sim 0.003$ s/km and dominate at $k < \sim 0.001$ s/km. The amplitude of the flux fluctuations will depend on the absolute flux level. Some sort of normalization is thus necessary if we want to use the flux power spectrum as measure of the fluctuations of the optical depth.

There are several ways to do that. Traditionally for a spectrum with high resolution and high S/N, such as our data, the continuum is estimated by interpolating regions of low absorptions with a stiff polynomial (see section 2.3). This is a reasonable thing to do as the continuum fluctuations dominate only on large scales. The power spectrum of the quantity

$$F1 = I_{\text{obs}}/I_{\text{em}} = e^{-\tau} \quad (2)$$

can then be calculated. However, the fluctuation amplitude will still depend on the mean optical depth in the spectrum, which is a strong function of redshift. Because of this Hui et al. (2001) suggested using the flux power spectrum of the quantity:

$$F2 = e^{-\tau} / \langle e^{-\tau} \rangle - 1 = F1 / \langle e^{-\tau} \rangle - 1. \quad (3)$$

The power spectrum of $F2$ is related to that of $F1$ by a constant factor $(\langle e^{-\tau} \rangle)^{-2}$.

Continuum fitting is a somewhat arbitrary and time-consuming procedure. We have thus also investigated the power spectrum of

$$F3 = I_{\text{obs}} / \langle I_{\text{obs}} \rangle - 1 = I_{\text{em}} e^{-\tau} / \langle I_{\text{em}} e^{-\tau} \rangle - 1, \quad (4)$$

where $\langle I_{\text{em}} e^{-\tau} \rangle$ is the average flux of the region of the spectrum used to calculate the power spectrum. $F3$ is easier to calculate and its flux power spectrum should become identical to that of $F2$ at small scales ($k > k_{\text{cont}}$) (see also C02).

To combine and compare spectra at different redshift it is convenient to introduce yet another estimate of the flux

$$F4 = e^{-\tau/B(z)}, \quad (5)$$

where $B(z)$ is a scaling factor which varies with redshift and is chosen in order to reproduce the mean flux at a given z . We will use $F4$ in section 4.2 to test the gravitational growth of Lyman- α forest structures. When the optical depth is in the range $0.05 \leq \tau \leq 5$, the observed optical depth can be reasonably well estimated from the normalized flux (Nusser & Haehnelt 1999). When τ is smaller the continuum fitting errors and noise result in an unreliable estimate of the optical depth. When lines are saturated, i.e. $\tau > 5$, the optical depth can in principle be estimated from higher order lines of the Lyman series but this is beyond the scope of this paper (see for example Aguirre et al. 2002). In saturated regions we leave the flux unchanged. Because of these problem in saturated regions and regions of low optical depth this will not work too well and $F4$ should be considered with caution.

In order to compute the 1D flux power spectrum, $P_F^{1D}(k)$, we use the following procedure: *i*) we cut the spectrum using the wavelength ranges indicated in Table 2; *ii*) we convert the wavelengths in velocity units assuming an Einstein-de Sitter Universe (e.g. M00); *iii*) we use a Lomb periodogram routine (Lomb 1976; Scargle 1982) to compute the power spectrum of unevenly sampled data.

For an isotropic distribution (Kaiser & Peacock 1991) the 3D power spectrum is obtained via numerical differentiation of the 1D power spectrum,

$$P^{3D}(k) = -\frac{2\pi}{k} \frac{d}{dk} P^{1D}(k). \quad (6)$$

Both peculiar velocities and thermal broadening make the flux field anisotropic and the 3D flux power spectrum will depend on the angle of the wavevector to the line-of-sight (Kaiser 1987, Hui 1999; McDonald & Miralda-Escudé 1999, McDonald 2003). Nevertheless P_F^{3D} calculated with eq. (6) from the 1D flux power spectrum is often referred to as 3D flux power spectrum. To remind the reader that eq. (6) does not give the true 3D power spectrum we will denote it as “3D” flux power spectrum throughout.

To allow a better comparison with previous work we will prefer to plot the dimensionless “3D” power spectrum,

$$\Delta_F^2(k) = \frac{1}{2\pi^2} k^3 P_F^{\text{“3D”}}(k), \quad (7)$$

which is the contribution to the variance of the flux per interval $d \ln k$.

C02 pointed out that the “3D” power spectrum depends on the resolution of the QSO spectra. Finite resolution results in a steepening of the 1D power spectrum. This results in an increase of the amplitude of the “3D” flux power spectrum which is obtained via differentiation.

3.2 Jackknife analysis of statistical errors

We use a jackknife estimate for the errors (Bradley 1982). The jackknife estimate of the 1σ uncertainty of a statistical quantity Y is obtained by dividing the sample into N subsamples and computing $\sigma = [\sum_{i=1}^N (Y_i - \bar{Y})^2]^{1/2}$, where \bar{Y} is the estimate from the full data sample and Y_i is the value estimated from the sample *without* the subsample i . There are two advantages in using the jackknife estimate rather than the more common bootstrap resampling techniques. Firstly, it can be obtained without any “randomization” of the sample. Secondly, it has been shown that jackknife estimates tend to reduce the bias which is of order $1/N$ where N is the number of measurements. Nevertheless, when we compared the two methods they give very similar results. In some cases, especially for small subsamples, we will show the 1σ dispersion of the distribution instead of the jackknife estimate. Note that jackknife estimates tend to underestimate the true errors.

3.3 Effects of continuum fitting and errors in the zero level of the flux

As apparent from eq. (1) the fluctuations of the flux distribution are a superposition of variations in the intervening absorption and variations in the intrinsic spectrum of the QSO (*i.e.* the continuum). As discussed in detail section 2.3 it is possible to remove most of these fluctuations with a “continuum fit” of the observed spectrum. However, for scales larger than $30-40 \text{ \AA}$ (this is the typical length of one echelle order) the continuum fluctuations start to strongly dominate and fundamentally limit the possibility of recovering the contribution from the intervening absorption (Hui et al. 2001). This is shown in Figure 2 where we have compared the flux power spectra for continuum fitted spectra ($F2$, eq. 3) and spectra without continuum fit ($F3$, eq. 4). As is clearly seen the continuum fluctuations start to contribute significantly on scales $k < k_{\text{cont}} \sim 0.003 \text{ s/km}$ and dominate at $k < k_{\text{cont}} \sim 0.001 \text{ s/km}$ while at smaller scale the flux power spectrum of the simple averaged quantity $F3$ is identical to that of the flux-normalized spectrum $F2$. The open triangles show the flux power spectrum of 22 of the 27 spectra for which the spectra covered the region $1265.67 - 1393.67 \text{ \AA}$ redwards of the Lyman- α emission line where there is no Lyman- α absorption. There is a very similar rise at $k < 0.003 \text{ s/km}$.

The continuum fit has the effect of filtering out fluctuation on scales larger than 30 \AA . To demonstrate this explicitly we show the flux power spectrum for $F3_{s25} = I_{\text{obs}} / \langle I_{\text{obs}} \rangle_{s25} - 1$ (and $F3_{s50}$) where $\langle I_{\text{obs}} \rangle_{s25}$ (and $\langle I_{\text{obs}} \rangle_{s50}$) are the observed intensity smoothed with a Gaussian window of 25 \AA (50 \AA) width (σ) as the solid (dashed) curve. At $k > 0.003 \text{ s/km}$ continuum fitting errors should thus play a very minor role. The time consuming and somewhat arbitrary procedure of continuum fitting is thus only necessary if the recovery of optical depth fluctuations on scales larger than this is attempted. In the following we will always take $F3_{s25}$ if we do not use continuum fitted spectra.

The conversion of velocity scale to physical length † is model-dependent. For our assumed cosmology ($\Omega_m = 0.3$, $\Omega_\Lambda = 0.7$) $k = 0.003 \text{ s/km}$ corresponds to a wavelength of $\sim 25 h^{-1}$ comoving Mpc at $z = 2.5$. The fact that the continuum fluctuations contribute significantly at scales larger than $25 h^{-1}$ comoving Mpc at $z = 2.5$ will make it difficult to recover the optical depth fluctuations and thus the matter density fluctuation with high accuracy on scales larger than this scale. This may, however, be easier with the cross-correlation of the flux of adjacent lines-of-sight as can be obtained from close QSO pairs. There the continuum fluctuations drop out because the continua of different QSOs will not be correlated on the relevant scales unless the QSOs are at very similar redshift (Viel et al. 2002a).

We have also investigated how the errors in zero level of the flux discussed in section 2.2. may affect the flux power spectrum. For this purpose we have set the flux to zero whenever the flux was below 0.05. The resulting flux power spectrum was different by less than 2 percent.

3.4 Effects of metal lines and DLAS

As discussed in section 2.4 the Lyman- α forest is “contaminated” by metal absorption lines. For 13 of the 27 spectra (see Table 2) we have identified metal lines and fitted them with VPFIT. From these line lists we have produced

† The different units are related by: $[k/(\text{km/s})^{-1}] = (1+z)/(\Omega_m(1+z)^3 + \Omega_k(1+z)^2 + \Omega_\Lambda)^{1/2} [k/h(\text{Mpc}^{-1})/100] = (1+z)/3 [k/\text{\AA}^{-1}]/82.23$.

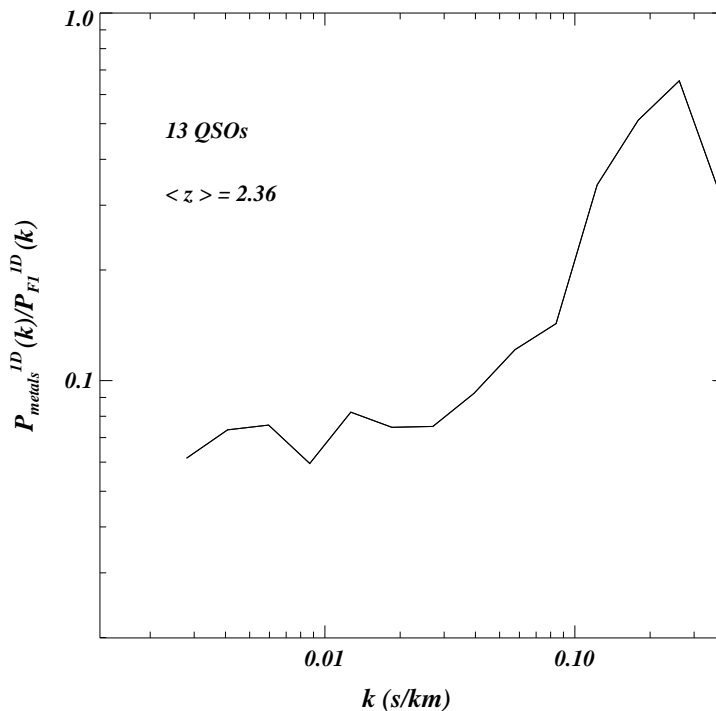


Figure 3. Effect of metal lines. The solid curve shows the metal line contribution to the total flux power spectrum of the Lyman- α forest region. Metal-line only spectra have been generated from the line lists of 13 QSOs fitted with VPFIT. The mean redshift of this subsample is $\langle z \rangle = 2.36$.

artificial spectra which contain the metal lines only. Figure 3 shows the mean flux power spectrum of these metal-line-only spectra divided by the mean flux power spectrum of the real spectra including metal lines. The contribution of metal lines reaches 50 % at small scales but drops to less than 10 % at large scales ($k < 0.1$ s/km). This agrees well with estimates of M00 and C02, who also found the metal line distribution to be small on scales larger than $k \sim 0.1$ s/km.

We are here mainly interested in the large scale flux power spectrum and thus in the following we will ignore the metal line contribution. In principle it is possible to remove the metal lines but this was not done because it can lead to windowing effects in the power spectrum on large scales where removal is not really necessary and will be difficult at small scales because of the rather large metal line contribution. Attempts to use the small scale cut-off to constrain the matter power spectrum and to determine physical parameters of the Lyman- α forest will need a very careful removal of the metal line contribution.

We have also computed the flux power spectrum with and without cutting out the damped Lyman- α systems. The results are consistent within the error bars but generally smaller without damped Lyman- α systems. The difference is less than 5% at large scales and drops to 2% for $k > 0.02$ s/km. Note that the sample contains only four (sub-)damped Lyman- α systems which we have cut out.

4 FLUX POWER SPECTRUM OF THE OBSERVED ABSORPTION SPECTRA

4.1 The total sample

In Figure 4 we show the 1D and “3D” power spectrum of the flux estimator $F1$ for the full sample. The spectra were continuum fitted as described in section 2.3 and no attempt has been made to remove metal lines. The 1D spectrum is remarkably smooth for $k > 0.005$ s/km. The errors were obtained with the jackknife estimator described in section 3.2. Figure 5 compares the “3D” power spectrum of the flux-normalized spectra ($F2$) and those of spectra smoothed with a 25 Å window. For $k < 0.007$ s/km the power spectrum of $F3_{s25}$ is still somewhat larger than that of $F2$ indicating that the smoothing window was too wide to remove the continuum fluctuations on these scales. Tables 3

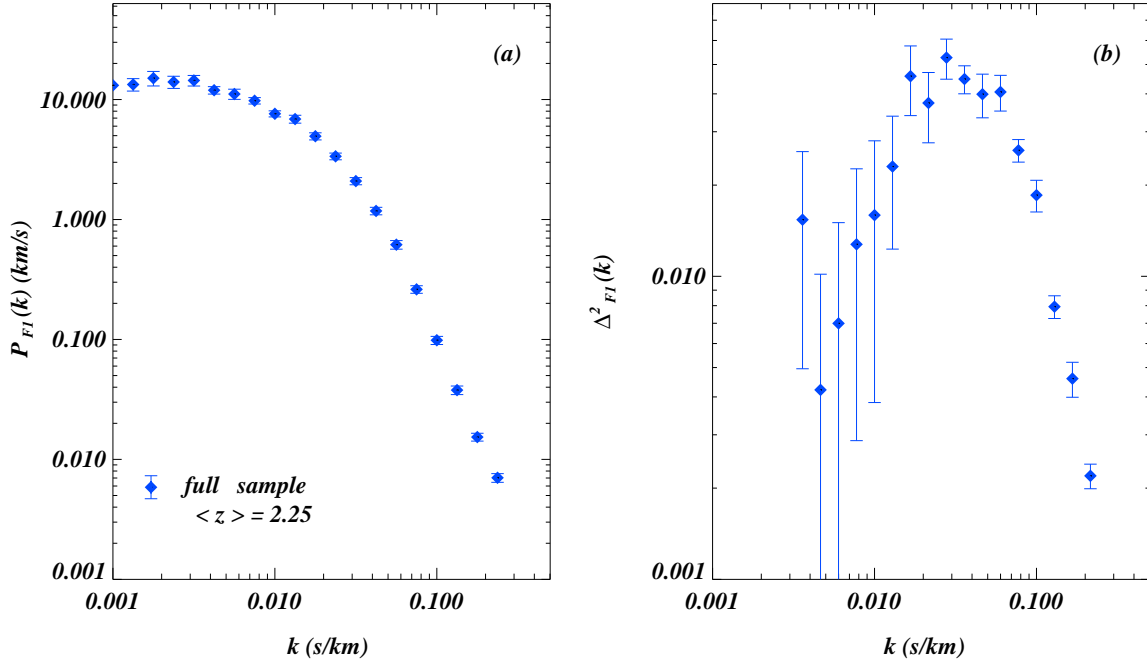


Figure 4. The 1D and “3D” flux power spectrum of the full sample for the flux estimator $F1 = \exp(-\tau)$. Errors bars are jackknife estimates. Note that the LUQAS points (diamonds) in the left panel are different from the one in the published version in Kim et al. (2004) MNRAS 347, 355 (where the k values of the 1D flux power spectrum had been erroneously shifted by half a bin size in $\log k$).

and 4 give the mean 1D and “3D” flux power spectrum of the full sample for the flux estimator $F1$, $F2$ and $F3$ as described in 3.1 and 3. The “3D” flux power spectrum was estimated by linearly connecting neighbouring points of an estimate of the 1D flux power spectrum binned with the same bin size but shifted by half a bin width. The bin size was chosen such that the visual comparison of different samples in the plots is not hindered by too large bin to bin fluctuations and varies for different (sub-)samples.

4.2 Redshift evolution

The flux power spectrum evolves strongly with redshift. It is thereby important to discriminate between changes due to evolution of the absolute emitted flux, the normalized flux and the optical depth. As discussed in more detail in section 6 it is the latter which is most directly related to the fluctuations of the matter density. Figure 6a shows the redshift evolution of the flux power spectrum for our standard estimator $F1$. The amplitude increases strongly with increasing redshift. As discussed in detail by C02 this is due to the increased mean optical depth at high redshift. The amplitude of the matter density fluctuations actually evolves in the opposite way. Figure 6b shows the evolution of 1D flux power spectrum for our estimator $F4$ where we have rescaled the optical depth of the observed spectra to have the same effective optical depth of $\tau_{\text{eff}} = -\ln \langle F1 \rangle = 0.15$, the mean value at redshift $z = 2$. Note that in Figure 6b we have plotted kP_F^{1D} and that the plot is linear. These rescalings are somewhat problematic because both very small and very large optical depths cannot be recovered correctly because of noise and saturation effects. Nevertheless it is encouraging that with the rescaling the evolution is now reversed and the amplitude increases with decreasing redshift as expected for the fluctuations of the matter density. In Tables 5 and 6 we list the values for the 1D and “3D” estimates of the flux power spectrum $F2$, in three different redshift ranges with mean redshift $\langle z \rangle = 1.87, 2.18, 2.58$.

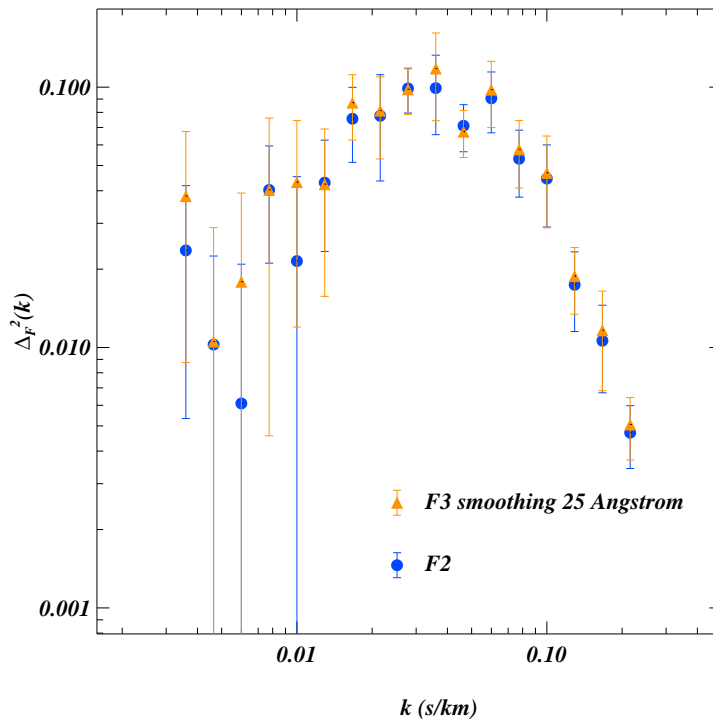


Figure 5. “3D” power spectrum of two different flux estimators. Circles are for $F2 = e^{-\tau} / \langle e^{-\tau} \rangle - 1$ calculated from continuum fitted spectra and triangles are for $F3_{s25} = I_{\text{obs}} / \langle I_{\text{obs}} \rangle_{s25} - 1$ calculated from not continuum fitted spectra. $F3$ is smoothed with a Gaussian window of width 25 Å. See Section 3 for details. Error bars are jackknife estimates calculated from the sample of 27 QSOs.

5 COMPARISON WITH PREVIOUS RESULTS

5.1 Amplitude and slope

We first compare the subsample of our spectra in the redshift range $1.6 < z < 2.3$ with subsample A of C02 where we have the biggest overlap in terms of number of QSO spectra. The 1D flux power spectra for the flux estimator $F2$ are in good agreement, within the errors, in the range of k not affected by differences in resolution and S/N (Figure 7a). The power spectrum of the LUQAS sample is somewhat smoother due to the larger number of QSO spectra in this redshift range. There is a slight “excess” of our sample at $k \sim 0.04$ s/km compared to the C02 sample. At the smallest scales the pixel noise in the spectra starts to dominate and at $k > 0.3$ s/km the effect of the about a factor two larger pixel noise in the Croft sample can be seen. Hui et al. (2001) gave a rough estimate of the pixel noise contribution to the flux power spectrum $\sim 2(\delta v / \bar{f})(S/N)^{-2}$, where δv is the pixel size, \bar{f} is the mean transmission and S/N is the signal-to-noise ratio. For the LUQAS sample with a pixel size of 2.5 km/s, $\bar{f} = 0.86$ and $S/N = 50$ the expected contribution to the flux power spectrum is 2.5×10^{-3} km s $^{-1}$ and thus below the plotted range.

In Figure 7b we compare the corresponding “3D” flux power spectra. The “3D” flux power spectra are also in good agreement and the amplitude is the same within the errors. As before the “3D” power spectrum is considerably noisier because of the differentiation procedure and we have thus chosen to compare our full sample to the full sample of C02 (Fig. 8a) in order to assess whether the LUQAS sample has the same slope at intermediate scales, where continuum fitting errors are not dominant and the flux power spectrum is not affected by thermal effects. The slope of $P_F^{\text{“3D”}}(k)$, at small k , for our sample appears to be somewhat shallower. To quantify this we have fitted a power law of the form:

$$P_F^{\text{“3D”}}(k) = P_F^{\text{“3D”}}(k_p) \left(\frac{k}{k_p} \right)^\nu, \quad (8)$$

to the “3D” flux power spectra.

Figure 8b shows the χ^2 distribution for a fit in the range $0.0035 < k \text{ (s/km)} < 0.02$. We have thereby followed the procedure in Croft et al. (2002). We have first performed a 2 parameter fit. We have then determined a pivot

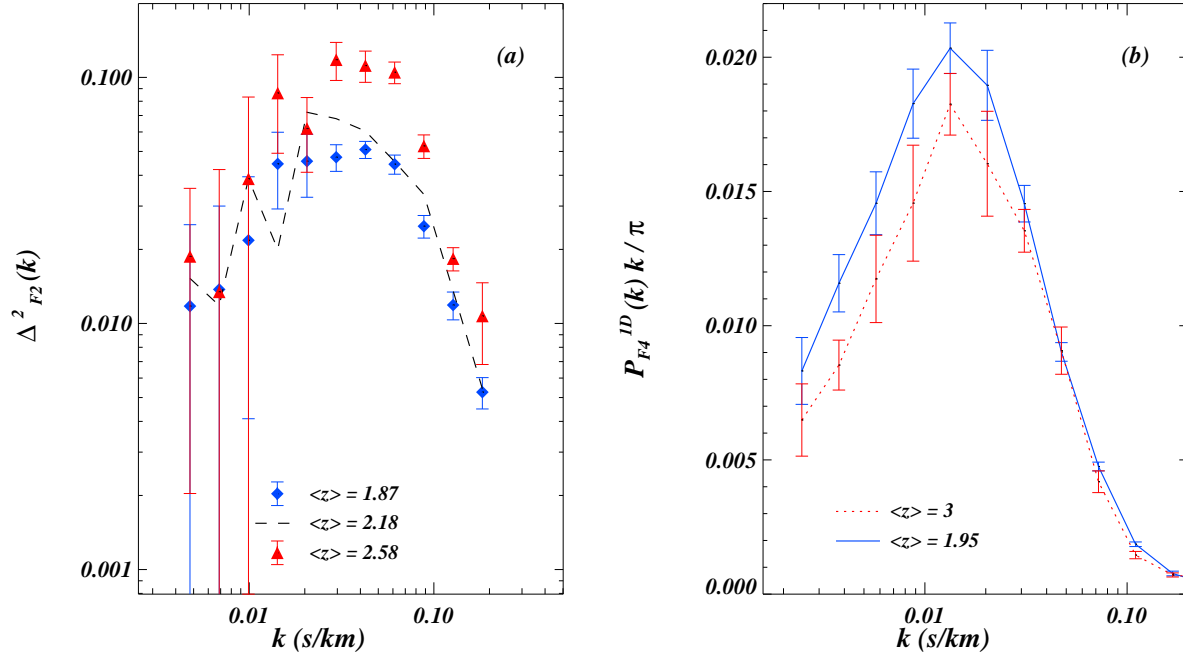


Figure 6. *Left:* Redshift evolution of the “3D” flux power spectrum of the flux estimator $F2 = e^{-\tau} / \langle e^{-\tau} \rangle - 1$: diamonds ($1.6 < z < 2$; $\langle z \rangle = 1.87$); dashed line ($2 < z < 2.4$; $\langle z \rangle = 2.18$); triangles ($2.4 < z < 2.8$; $\langle z \rangle = 2.58$). *Right:* Redshift evolution of the dimensionless 1D flux power spectrum kP_F^{1D} after rescaling of the optical depth such that $\tau_{eff} = 0.15$ at $z = 2$ for all spectra (flux estimator F4) and for two different mean redshift of $\langle z \rangle = 1.95$ (continuous line) and $\langle z \rangle = 3$ (dotted line). Note that the flux power spectrum now increases with decreasing redshift as expected for gravitational growth. Errors are jackknife estimates.

wavenumber for which the amplitude and slope are uncorrelated ($k = 0.015$ s/km for our sample and that of C02) and varied the slope keeping the amplitude at the best fitting value of the 2 parameter fit. The resulting χ^2 is shown in Figure 8b. The logarithmic slope of $P_F^{3D}(k)$ for the LUQAS sample is 0.3 shallower than that of the C02 sample, although the results are compatible within 1σ errors. Note also that the median redshift of our sample is somewhat lower than that of C02 and that the largest scale used in the fit may already be slightly affected by continuum fitting (see Figures 2 and 5).

5.2 Redshift evolution

In Figure 9 we compare the evolution of the dimensionless 1D power spectrum for the flux estimator $F1$ of our three subsamples with that of M00. The agreement is again good at the redshifts covered by the M00 sample. Note that we follow M00 and plot kP_F^{1D} and that the plot is linear. The observed decrease of the flux power spectrum of the LUQAS sample which extends to lower redshift continues. The flux power spectra of the M00 sample are somewhat noisier because of the smaller number of QSO spectra. In section 4.3 we had demonstrated that the amplitude of the flux power spectrum of our sample increases with decreasing redshift once we rescaled the optical depth. Such a growth is expected if the matter fluctuations grow. C02 found that their recovered linear matter power spectrum was consistent with gravitational growth.

Our attempt to rescale our spectra to the mean optical depth of the M00 did not give reasonable results. This is most likely due to the fact that a rescaling of the optical depth by large factors does not work because recovering the optical depth at small and large values is significantly limited by noise/continuum fitting errors and saturation effects, respectively. A direct comparison of rescaled spectra with the M00 results was thus not possible.

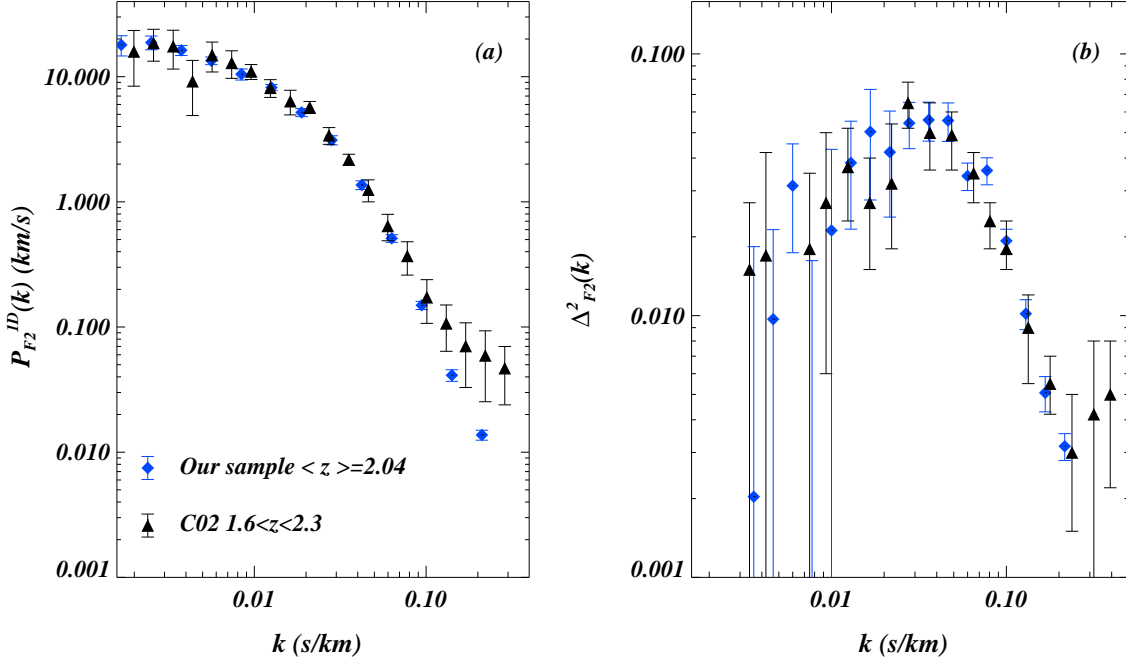


Figure 7. Comparison with Croft et al. 2002 (C02) results. *Left:* 1D power spectrum of $F2 = e^{-\tau} / \langle e^{-\tau} \rangle - 1$ for our sample in the redshift range $1.6 < z < 2.3$, with a $\langle z \rangle = 2.04$, (diamonds) and the C02 results for their subsample A in the same redshift range (triangles). *Right:* “3D” flux power spectrum (plotted in dimensionless units) for the two samples on the left. Error bars are jackknife estimates. Note that the LUQAS points (diamonds) in the left panel are different from the one in the published version in Kim et al. (2004) MNRAS 347, 355 (where the k values of the 1D flux power spectrum had been erroneously shifted by half a bin size in $\log k$).

6 FROM THE FLUX POWER SPECTRUM TO THE MATTER POWER SPECTRUM AND COSMOLOGICAL PARAMETERS

In the fluctuating Gunn-Peterson approximation the relation between the absorption optical depth and matter density in redshift space can be written as

$$\tau = A \left(\frac{\rho}{\langle \rho \rangle} \right)^\alpha \quad (9)$$

where $1.6 \lesssim \alpha \lesssim 2$ depend on the temperature density relation of the gas (see Weinberg et al. 1999 for a review). For small fluctuation

$$\frac{dF}{\langle F \rangle} = -A \alpha \delta, \quad (10)$$

where $1 + \delta = \rho / \langle \rho \rangle$. On large scales the flux power spectrum should thus, up to a constant factor, be identical to the matter power spectrum in redshift space. Unfortunately even on large scales this is complicated due to peculiar velocity effects and the presence of non-linear structures which lead to saturated absorption. Viel et al. (2003b) find that strong discrete absorption systems contribute significantly ($\gtrsim 50\%$) to the flux power spectrum at large scales. The relation between the flux and matter power spectrum is thus more complicated. C99, C02 and M00 have used numerical simulations to determine the normalization and slope of the real space matter power spectrum from the flux power spectrum. The samples have different redshift distributions and resolution. It is thus not completely straightforward to compare the results. After suitable rescaling in k and redshift C02 found good agreement with M00 and a 25 % smaller fluctuation amplitude and a 0.1 shallower logarithmic slope of the matter power spectrum than C99. Without numerical simulations we are not able to directly infer the amplitude and slope of the linear matter power spectrum. However, the amplitude of the flux power spectrum is in good agreement with that of C02 and M00 and the inferred matter fluctuation amplitude should be the same. We have obtained a 0.3 shallower logarithmic slope for $P_F^{3D}(k)$ but the errors are large and the results are consistent with that of Croft et al. within 1σ . The recent combined analysis of the WMAP results with the C02 has claimed that shape and amplitude of the matter

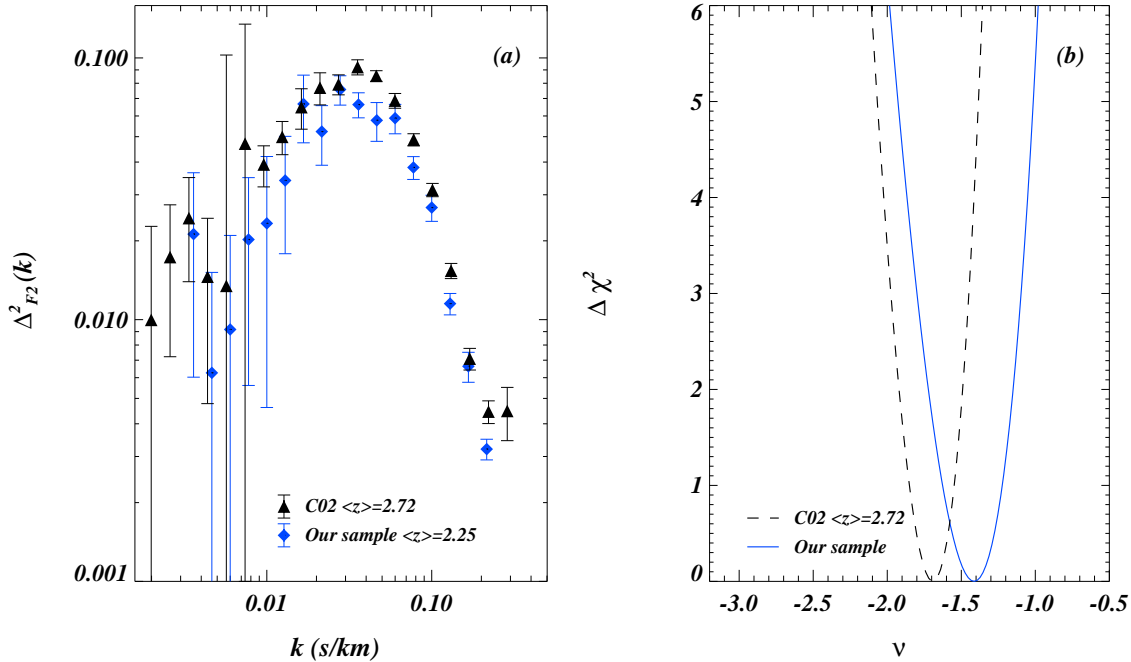


Figure 8. *Left:* Comparison of the “3D” power spectrum of our full sample and that of C02. *Right:* χ^2 distribution for the logarithmic slope of a power law fit to the flux power spectrum, $P_F^{“3D”}(k)$, in the left panel. The range of wavenumbers fitted is $0.0035 < k$ (s/km) < 0.02 and we fix the amplitude of our fit (eq. 8) to the best fitting value at $k = 0.015$ s/km.

power spectrum inferred by C02 is not consistent with a scale invariant initial fluctuation spectrum (Bennet et al. 2003, Spergel et al. 2003, Verde et al. 2003). However, as discussed in the introduction, it has been argued that the errors of amplitude and slope of the matter power spectrum have been underestimated and that this discrepancy is not significant (Zaldarriaga, Soccimarro & Hui, 2003; Zaldarriaga, Hui & Tegmark, 2001; Gnedin & Hamilton 2002; Seljak, McDonald & Makarov 2003).

7 CONCLUSIONS

We have calculated the flux power spectrum for a new large sample of high resolution high signal-to-noise QSO absorption spectra taken with the ESO-UVES spectrograph and compared it to previous published flux power spectra. Our conclusions can be summarized as follows.

1. The flux variation Δ_F^2 rises from 0.01 at $k \sim 0.003$ s/km to 0.1 at $k \sim 0.03$ s/km and drops rapidly at larger k .
2. At $k < 0.003$ s/km the flux power spectrum is strongly dominated by continuum fluctuations while at $k > 0.003$ s/km the results for continuum fitted spectra and simply averaged spectra are very similar.
3. The metal line contribution to the flux power spectrum is less than 10 % at scales $k < 0.01$ s/km and rises to 50 % at smaller scales.
4. The agreement with the studies of Croft et al. (2002 - C02) and McDonald et al. (2000 - M00) is good. The amplitude of the flux power spectrum at the peak is the same as that in the sample of C02 and M00 within the errors. The logarithmic slope for the flux power spectrum $P_F^{“3D”}(k)$ at small k is 0.3 shallower than that of C02 but consistent within 1σ .
5. The amplitude of the power spectrum rises with increasing redshift due to the increasing mean flux. After correcting to the same mean flux the fluctuation amplitude decreases with increasing redshift as expected from gravitational clustering.

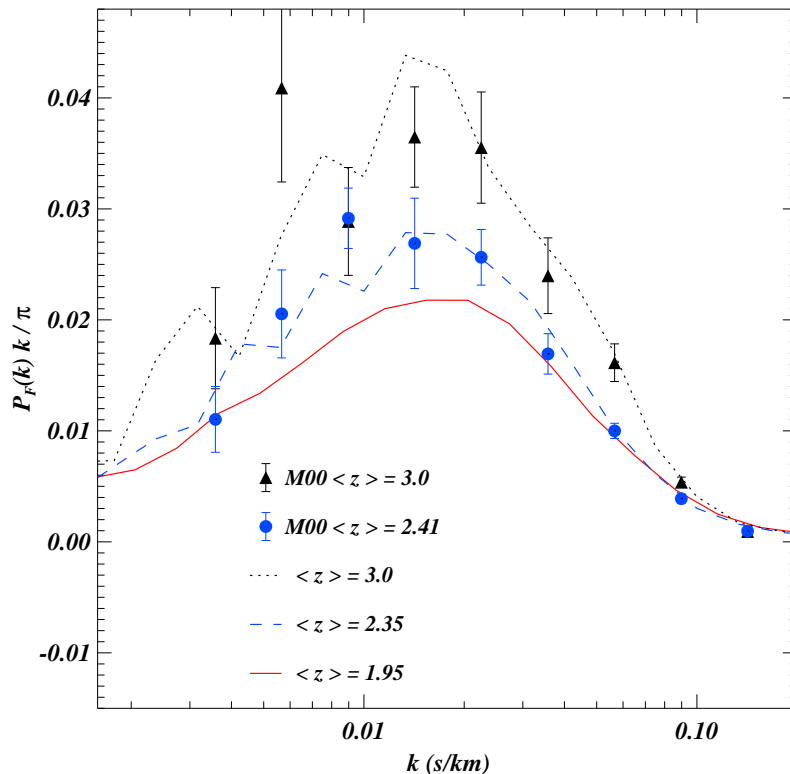


Figure 9. Comparison of redshift evolution to McDonald et al. 2000. Plotted is the dimensionless 1D power spectrum kP_F^{1D} for three different subsamples of our data set: $1.75 < z < 2.15$ ($\langle z \rangle = 1.95$, continuous line), $2.15 < z < 2.65$ ($\langle z \rangle = 2.35$, dashed line) and $2.75 < z < 3.25$ ($\langle z \rangle = 3.0$, dotted line). The results of McDonald et al. 2000 (M00) at two different redshifts are shown as circles ($z = 2.41$) and triangles ($z = 3.0$).

ACKNOWLEDGMENTS.

This work was supported by the European Community Research and Training Network “The Physics of the Inter-galactic Medium”. We would like to thank ESO, the ESO staff, the ESO science verification team and the team of the UVESLP “QSO absorption lines” for initiating, compiling and making publicly available a superb set of QSO absorption spectra. Last but not least we would like to thank the UVES team for building the spectrograph. TSK would like to thank Michael Rauch for his advice on continuum fitting. We thank the anonymous referee for his very helpful report and D. Weinberg for useful discussions.

REFERENCES

- Aguirre A., Schaye J., Theuns T., 2002, ApJ, 576, 1
 Bi H.G., Davidsen A.F., 1997, ApJ, 479, 523
 Cen R. Miralda-Escude J., Ostriker J. P., Rauch M., 1994, ApJ, 437, L9
 Bennett C.L. et al., 2003, astro-ph/0302207
 Bradley E., 1982, “The jackknife, The Bootstrap and other resampling plans”, Philadelphia, SIAM
 Croft R.A.C., Weinberg D. H., Katz N., Hernquist L., 1998, ApJ, 495, 44
 Croft R.A.C., Hu W., Davé R., 1999a, PhRvL, 83, 1092
 Croft R.A.C., Weinberg D. H., Pettini M., Hernquist L., Katz N., 1999b, ApJ, 520, 1 (C99)
 Croft R.A.C., Weinberg D. H., Bolte M., Burles S., Hernquist L., Katz N., Kirkman D., Tytler D., 2002, ApJ, 581, 20 (C02)
 Davé R. et al. 1999, ApJ, 511, 521
 Elgaroy O. et al., 2002, PhRvL, 89, 1301
 Gnedin N.Y., Hui L., 1998, MNRAS, 296, 44
 Gnedin N.Y., Hamilton A.J.S., 2002, MNRAS, 334, 107
 Gunn J.E., Peterson B. A., 1965, ApJ, 142, 1633
 Hernquist L., Katz N., Weinberg D.H., Miralda-Escudé, 1996, ApJ, 457, L51

- Hui L., 1999, ApJ, 516, 519
Hui L., Burles S., Seljak U., Rutledge R. E., Magnier E., Tytler D., 2001, ApJ, 552, 15
Kaiser N., 1987, MNRAS, 227, 1
Kaiser N., Peacock J.A., 1991, ApJ, 379, 482
Kujat J. et al. 2002, ApJ, 572, 1
Lomb N.R., 1976, AP&SS, 39, 447
Kim, T.-S., Cristiani, S., D’Odorico, S. 2001, A&A, 373, 757
Kim, T.-S., Carswell, R. F., Cristiani, S., D’Odorico, S., Giallongo, E. 2002, MNRAS, 335, 555
Matarrese S., Mohayaee R., 2002, MNRAS, 329, 37
McDonald P., Miralda-Escudé J., 1999, ApJ, 518, 24
McDonald P., Miralda-Escudé J., Rauch M., Sargent W.L., Barlow T.A., Cen R., Ostriker J.P., 2000, ApJ, 543, 1 (M00)
McDonald P., 2003, ApJ, 585, 34
Meiksin A., Bryan G., Macachacek M., 2001, MNRAS, 327, 296
Miralda-Escudé J. et al. 1996, ApJ, 471, 582
Narayanan V.K., Spergel D.N., Davé R., Ma C.-P., 2000, ApJ, 543, 103
Nusser A., Haehnelt M.G., 1999, MNRAS, 303, 179
Phillips J., Weinberg D.H., Croft R.A.C., Hernquist L., Katz N., Pettini M., 2001, 560, 15
Rauch M., 1998, ARA&A, 36, 267
Seljak U., Mandelbaum R., McDonald P., 2002, astro-ph/0212343
Seljak U., McDonald P., Makarov A., 2003, astro-ph/0302571
Scargle J.D., 1982, ApJ, 263, 835
Spergel D.N. et al. 2003, astro-ph/0302209
Theuns T. et al. 1998, MNRAS, 301, 478
Theuns T., Viel M., Kay S., Schaye J., Carswell B., Tzanavaris P., 2002, ApJ, 578, L5
Verde L. et al. 2003, astro-ph/0302218
Viel M., Matarrese S., Mo H.J., Haehnelt M.G., Theuns T., 2002a, MNRAS, 329, 848
Viel M., Matarrese S., Mo H.J., Theuns T., Haehnelt M.G., 2002b, MNRAS, 336, 685
Viel M., Matarrese S., Theuns T., Munshi D., Wang Y., 2003, MNRAS, 340, L47
Viel M., Haehnelt M.G., Carswell R.F., Kim T.-S., 2003b, submitted to MNRAS, astro-ph/0308078
Viel M., Matarrese S., Heavens A., Haehnelt M.G., Kim T.-S., Springel V., Hernquist L., 2003c, submitted to MNRAS, astro-ph/0308151
Weinberg D. et al., 1999, in: Evolution of large scale structure : from recombination to Garching, eds. A. J. Banday, R. K. Sheth, L. N. da Costa., p.346
Zaldarriaga M., Hui L., Tegmark M., 2001, ApJ, 557, 519
Zaldarriaga M., Scoccimarro R., Hui L., 2003, ApJ, 590, 1
Zhang Y., Anninos P., Norman M.L., 1995, ApJ, 453, L57

Table 3. Mean 1D flux power spectrum of the full sample ($\langle z \rangle = 2.25$) for different flux estimators ^a

k (s/km)	$P_{F1}(k)$ (km/s)	$P_{F2}(k)$ (km/s)	$P_{F3}(k)$ (km/s)
0.0010	13.0770 \pm 2.1244	25.9785 \pm 6.6807	47.6964 \pm 16.1311
0.0013	13.7172 \pm 1.5985	25.8181 \pm 5.3323	35.9422 \pm 5.9444
0.0018	15.7603 \pm 2.1502	29.7464 \pm 6.0253	35.8427 \pm 6.9350
0.0024	14.5357 \pm 1.6421	25.8690 \pm 4.2306	33.7291 \pm 6.7301
0.0032	14.8066 \pm 1.3860	27.9988 \pm 5.5553	32.3716 \pm 6.6544
0.0042	12.4382 \pm 0.7775	23.0850 \pm 4.1762	25.3903 \pm 6.5073
0.0056	11.5405 \pm 1.0521	22.2407 \pm 4.5617	23.3662 \pm 6.6347
0.0075	9.8115 \pm 0.6149	18.3001 \pm 2.7549	19.4855 \pm 3.5507
0.0100	7.7051 \pm 0.4625	14.7067 \pm 2.6998	15.0972 \pm 2.7572
0.0133	7.0616 \pm 0.4988	13.2415 \pm 2.3227	12.9928 \pm 2.5944
0.0178	4.9893 \pm 0.3464	9.7117 \pm 1.9065	10.2946 \pm 2.2990
0.0237	3.4304 \pm 0.2170	7.0356 \pm 1.7857	7.0597 \pm 1.8803
0.0316	2.1377 \pm 0.1390	4.3820 \pm 1.1375	4.5441 \pm 1.3845
0.0422	1.2155 \pm 0.0786	2.4105 \pm 0.5488	2.3807 \pm 0.6219
0.0562	0.6369 \pm 0.0483	1.3610 \pm 0.4058	1.4009 \pm 0.5125
0.0750	0.2686 \pm 0.0180	0.5670 \pm 0.1649	0.5864 \pm 0.2019
0.1000	0.1008 \pm 0.0074	0.2230 \pm 0.0752	0.2403 \pm 0.0890
0.1334	0.0389 \pm 0.0030	0.0817 \pm 0.0245	0.0889 \pm 0.0286
0.1778	0.0157 \pm 0.0011	0.0309 \pm 0.0075	0.0355 \pm 0.0087
0.2371	0.0071 \pm 0.0006	0.0134 \pm 0.0026	0.0158 \pm 0.0027

a The different flux estimators: $F1 = \exp(-\tau)$; $F2 = e^{-\tau} / \langle e^{-\tau} \rangle - 1$, with $\langle e^{-\tau} \rangle$ the mean flux level for each QSOs; $F3_{s25} = I_{\text{obs}} / \langle I_{\text{obs}} \rangle_{s25} - 1$. Note that $F1$ and $F2$ are computed from continuum fitted spectra, while $F3_{s25}$ is calculated from not continuum fitted spectra smoothed with a Gaussian window of 25 Å width. See Section 3.3 for more details. Note that this table is different from the one in the published version in Kim et al. (2004) MNRAS 347, 355 (where the k values of the 1D flux power spectrum had been erroneously shifted by half a bin size in $\log k$). A machine-readable version of this table is available at <http://www.ast.cam.ac.uk/~rtnigm/luqas.htm>.

Table 4. Mean 3D flux power spectrum of the full sample ($\langle z \rangle = 2.25$) for different flux estimators ^a

k (s/km)	$\Delta_{F1}^2(k)$	$\Delta_{F2}^2(k)$	$\Delta_{F3}^2(k)$
0.0036	0.0154 \pm 0.0108	0.0236 \pm 0.0183	0.0381 \pm 0.0294
0.0046	0.0044 \pm 0.0064	0.0103 \pm 0.0122	0.0105 \pm 0.0183
0.0060	0.0074 \pm 0.0084	0.0061 \pm 0.0148	0.0179 \pm 0.0213
0.0077	0.0181 \pm 0.0101	0.0403 \pm 0.0192	0.0403 \pm 0.0357
0.0100	0.0116 \pm 0.0109	0.0215 \pm 0.0238	0.0432 \pm 0.0312
0.0129	0.0237 \pm 0.0116	0.0430 \pm 0.0196	0.0424 \pm 0.0267
0.0167	0.0498 \pm 0.0134	0.0756 \pm 0.0242	0.0871 \pm 0.0245
0.0215	0.0347 \pm 0.0094	0.0776 \pm 0.0340	0.0813 \pm 0.0283
0.0278	0.0527 \pm 0.0070	0.0989 \pm 0.0193	0.0981 \pm 0.0195
0.0359	0.0464 \pm 0.0052	0.0992 \pm 0.0335	0.1179 \pm 0.0436
0.0464	0.0409 \pm 0.0068	0.0711 \pm 0.0146	0.0675 \pm 0.0138
0.0599	0.0416 \pm 0.0053	0.0906 \pm 0.0238	0.0978 \pm 0.0279
0.0774	0.0272 \pm 0.0025	0.0531 \pm 0.0153	0.0577 \pm 0.0167
0.1000	0.0189 \pm 0.0021	0.0445 \pm 0.0155	0.0469 \pm 0.0180
0.1292	0.0082 \pm 0.0007	0.0174 \pm 0.0059	0.0188 \pm 0.0054
0.1668	0.0048 \pm 0.0006	0.0106 \pm 0.0039	0.0116 \pm 0.0048
0.2154	0.0023 \pm 0.0002	0.0047 \pm 0.0013	0.0051 \pm 0.0014

a The different flux estimators: $F1 = \exp(-\tau)$, $F2 = e^{-\tau} / \langle e^{-\tau} \rangle - 1$, $F3_{s25} = I_{\text{obs}} / \langle I_{\text{obs}} \rangle_{s25} - 1$. Note that $F1$ and $F2$ are computed from continuum fitted spectra, while $F3_{s25}$ is calculated from not continuum fitted spectra smoothed with a Gaussian window of 25 Å width. See Section 3.3 for more details. A machine-readable version of this table is available at <http://www.ast.cam.ac.uk/~rtnigm/luqas.htm>.

Table 5. 1D Flux power spectrum for $F^2 = \exp(-\tau) / \langle \exp(-\tau) \rangle - 1$ in three different redshift ranges ^a

k (s/km)	$P_{F^2}(k)$ (km/s) $\langle z \rangle = 1.87$	$P_{F^2}(k)$ (km/s) $\langle z \rangle = 2.18$	$P_{F^2}(k)$ (km/s) $\langle z \rangle = 2.58$
0.0010	26.3677 ± 8.3099	14.2952 ± 4.0715	9.9894 ± 3.3723
0.0013	26.2042 ± 7.0032	22.3200 ± 11.3997	33.3230 ± 10.7060
0.0018	18.0914 ± 4.9298	16.8461 ± 2.4814	46.9632 ± 19.5921
0.0024	19.2437 ± 6.1694	15.5272 ± 2.4619	23.3280 ± 5.3857
0.0032	18.6062 ± 4.0084	18.5186 ± 4.0294	33.7688 ± 10.1441
0.0042	13.8969 ± 2.2267	17.0164 ± 3.2064	21.2278 ± 2.6202
0.0056	13.0126 ± 1.4421	14.0088 ± 1.6224	23.6721 ± 4.1560
0.0075	11.1447 ± 1.7044	12.9511 ± 2.4550	21.2667 ± 4.3868
0.0100	9.7740 ± 1.1599	9.2170 ± 0.9704	15.7910 ± 2.4561
0.0133	6.5832 ± 0.5700	9.1975 ± 0.8948	13.5331 ± 1.5505
0.0178	4.8737 ± 0.5387	6.4600 ± 0.4893	10.3522 ± 1.1515
0.0237	3.3942 ± 0.3616	4.2577 ± 0.3428	7.8964 ± 0.9131
0.0316	2.3183 ± 0.1674	2.4256 ± 0.1518	4.4644 ± 0.3660
0.0422	1.1390 ± 0.1046	1.4664 ± 0.1074	2.7588 ± 0.2459
0.0562	0.6504 ± 0.0399	0.7202 ± 0.0418	1.2996 ± 0.0980
0.0750	0.2855 ± 0.0214	0.3304 ± 0.0244	0.5284 ± 0.0499
0.1000	0.1197 ± 0.0097	0.1213 ± 0.0094	0.2002 ± 0.0164
0.1334	0.0535 ± 0.0042	0.0490 ± 0.0060	0.0827 ± 0.0176
0.1778	0.0241 ± 0.0026	0.0199 ± 0.0022	0.0335 ± 0.0062
0.2371	0.0117 ± 0.0011	0.0089 ± 0.0009	0.0143 ± 0.0029

a Note that this table is different from the one in the published version in Kim et al. (2004) MNRAS 347, 355 (where the k values of the 1D flux power spectrum had been erroneously shifted by half a bin size in $\log k$). A machine-readable version of this table is available at <http://www.ast.cam.ac.uk/~rtnigm/luqas.htm>.

Table 6. “3D” Flux power spectrum for $F^2 = \exp(-\tau) / \langle \exp(-\tau) \rangle - 1$ in three different redshift ranges ^a

k (s/km)	$\Delta_{F^2}^2(k)$ $\langle z \rangle = 1.87$	$\Delta_{F^2}^2(k)$ $\langle z \rangle = 2.18$	$\Delta_{F^2}^2(k)$ $\langle z \rangle = 2.58$
0.0048	0.0118 ± 0.0134	0.0152 ± 0.0255	0.0187 ± 0.0167
0.0069	0.0137 ± 0.0163	0.0118 ± 0.0106	0.0134 ± 0.0288
0.0099	0.0218 ± 0.0177	0.0387 ± 0.0151	0.0387 ± 0.0445
0.0143	0.0445 ± 0.0153	0.0200 ± 0.0125	0.0864 ± 0.0372
0.0205	0.0456 ± 0.0131	0.0721 ± 0.0133	0.0620 ± 0.0208
0.0296	0.0474 ± 0.0059	0.0680 ± 0.0075	0.1180 ± 0.0208
0.0426	0.0509 ± 0.0041	0.0605 ± 0.0069	0.1117 ± 0.0162
0.0613	0.0444 ± 0.0040	0.0455 ± 0.0035	0.1048 ± 0.0106
0.0883	0.0248 ± 0.0026	0.0335 ± 0.0031	0.0526 ± 0.0058
0.1271	0.0119 ± 0.0015	0.0136 ± 0.0015	0.0183 ± 0.0020
0.1830	0.0053 ± 0.0008	0.0054 ± 0.0008	0.0107 ± 0.0039

a A machine-readable version of this table is available at <http://www.ast.cam.ac.uk/~rtnigm/luqas.htm>.